Available online at www.sciencedirect.com

ScienceDirect

Current Opinion in Electrochemistry

Review Article

Key concepts for understanding alkaline oxygen evolution reaction at the atomic/molecular scale

Yoon Jun Son[1], Kenta Kawashima[2], Raúl A. Márquez[2], Lettie A. Smith[2], Chikaodili E. Chukwuneke[2] and C. Buddie Mullins[1,2,3,4,5]

Abstract

Understanding and improving the sluggish oxygen evolution reaction (OER) is critical for efficient water electrolysis. However, given that the OER is a multi-step, inner-sphere electrochemical reaction, understanding the OER at the atomic/molecular scale is difficult due to its complex redox chemistry and convoluted reaction mechanism. Moreover, recent discoveries of new types of active site, active species, reaction mechanism, and the driving force of the OER further complicate our understanding of the OER. Herein, a review of the key concepts of the OER at the atomic/molecular scale is given, focusing on providing their clear definitions, principles, categories, and commonalities and differences. Also, the role of each concept in determining the OER activity is discussed.

Addresses

[1] McKetta Department of Chemical Engineering, The University of Texas at Austin, Austin, TX, 78712, USA
[2] Department of Chemistry, The University of Texas at Austin, Austin, TX, 78712, USA
[3] Texas Materials Institute, The University of Texas at Austin, Austin, TX, 78712, USA
[4] Center for Electrochemistry, and The University of Texas at Austin, Austin, TX, 78712, USA
[5] H2@UT, The University of Texas at Austin, Austin, TX, 78712, USA

Corresponding author: Mullins, C. Buddie (mullins@che.utexas.edu)

Current Opinion in Electrochemistry 2023, **39**:101298

This review comes from a themed issue on **Energy Transformation (2023)**

Edited by **Yung-Eun Sung** and **Dong Young Chung**

For a complete overview see the Issue and the Editorial

Available online 14 April 2023

https://doi.org/10.1016/j.coelec.2023.101298

Keywords

Oxygen evolution reaction, Redox center, Active site, Active species, Reaction mechanism, Driving force.

Introduction

For efficient water electrolysis, enhancing the sluggish kinetics of the oxygen evolution reaction (OER) is crucial. While noble metal-based oxide electrocatalysts (*e.g.*, IrO_x and RuO_x) show the benchmark OER activity in acidic electrolytes, their high cost and scarcity hinder their large-scale applications [1,2]. In this regard, alkaline OER has gained great attention because low-cost and earth-abundant materials, such as 3d-transition metals (*e.g.*, Ni, Co, and Fe), can be employed as OER electrocatalysts with promising activity and stability [3–8].

To improve the kinetics of OER electrocatalysis, an in-depth understanding of the OER and the underlying principle determining the activity of the OER electrocatalyst is required. However, both are difficult to understand because the OER has complex redox chemistry and convoluted reaction mechanisms at the atomic/molecular scale due to its multi-step, inner-sphere electrochemical reaction that involves a four-electron transfer and the breaking/formation of chemical bonds [9].

From the conventional viewpoint, the OER occurs on the metal active site with cation redox chemistry, and the reactant from the electrolyte is consumed to produce O_2 gas. Also, the OER is directly driven by increasing the electrostatic potential with an applied bias [9]. However, recent development of *in situ* or *operando* characterization techniques enables the observation of the surface state of the electrocatalyst during the OER. This leads to the discovery of new types of active sites and redox chemistries (*e.g.*, oxygen active site with anion redox chemistry) [10], active species (*e.g.*, negatively charged oxygen species, electrophilic oxygen, and electrophilic metal–oxygen species) [11–13], reaction mechanisms (*e.g.*, participation of lattice oxygen for the OER) [10], and driving forces (*e.g.*, chemical potential) for the OER [12,14].

This review aims to present an overall understanding of the alkaline OER at the atomic/molecular scale. To this end, several key concepts for the OER are discussed, such as the active phase, active site, redox center, electronic structure, active species, reaction mechanism, rate-determining step (RDS), and driving force for this electrochemical reaction. This review provides clear definitions, principles, categories, and correlations

of these key concepts. Also, the role of each concept in determining the OER activity is discussed.

Active phase, active site, and active species

For alkaline OER, late 3d-transition metal (M, such as Ni, Co, and Fe)-based materials have been mainly utilized as OER electrocatalysts [3,4]. However, these metals, metal oxides (*e.g.*, rock salt, spinel, perovskite, layered oxide, and layered (oxy)hydroxide), and metalloids (*e.g.*, carbides, pnictides, chalcogenide, and halides) act as precatalysts that undergo irreversible electrochemical oxidation and structure reconstruction during the OER, forming a surface layer consisting of an active phase of hydrous metal (oxy)hydroxides (MO_xH_y), as depicted in Figure 1a [5,15–17]. Here, the active phase is defined as the crystal phase or structure (including amorphous structure) on the grain-size scale that exists during the OER. The MO_xH_y active phase has an edge-sharing octahedral structure with each metal and oxygen atom coordinated to six oxygen and three metal atoms, respectively [18–21].

Once the active phase is formed, understanding the identity of active sites on the atomic scale is critical for comprehending the OER mechanism and activity. The OER active site on the active phase of MO_xH_y can be either a metal site, oxygen site, or M–O motif [10,12] and these active sites can participate in the OER *via* single site or dual (or multi) sites mechanism (Figure 1b) [8,22–24]. These active sites are usually located on edge or defect sites that have a coordination number of less than six and three for the metal and oxygen site, respectively, and thus have proper adsorption energies for OER intermediates [25,26]. The identity of active sites can be investigated by *operando* X-ray absorption spectroscopy (XAS) and density functional theory (DFT) calculations [22,24,27]. *Operando* XAS analysis provides the atomic and electronic structure information (*e.g.*, oxidation state, bond distance, and coordination) of catalysts during the OER. Based on this structural information, DFT can calculate the theoretical catalytic activity of each candidate active site. Additionally, scanning electrochemical microscopy can be used to identify the active site by quantitatively correlating the density of active sites and catalytic activity [28].

Each type of active site on the active phase undergoes *in situ* redox chemistry during the OER and dynamically forms an active species that has a unique chemical structure (*e.g.*, composition, spatial arrangement, chemical bonds, and overall charge) and redox properties (*e.g.*, redox centers and redox states) [11,12,14,25]. It is noted that OER active sites show redox activity, but not all redox centers can be active sites. Active species is defined as (1) the active site or (2) the active site–reaction intermediate surface complex with a certain redox nature or certain overall charge in the rate-determining step (RDS) of the OER. Note that during the OER process, every component of the active species except for hydrogen must undergo redox reactions or charge accumulation before or during the RDS. Active species acts as the precursor for the OER, and its nature and surface coverage (θ) on the catalyst determine the overall OER activity.

The detection of the active species and the identification of their chemical structure can be performed by employing *in situ* spectroscopies including *in situ* ultraviolet-visible (UV-Vis) spectroscopy [3,19,29–31], Raman spectroscopy [4,11,19,31–33], X-ray photoelectron spectroscopy (XPS) [34,35], and X-ray absorption near edge spectroscopy (XANES) [13,19,31,35]. Here, selective detection of active species is possible for the following reason.

In situ spectroscopy can detect the reaction intermediates that have a relatively long lifetime with discernible accumulation, which corresponds to those of preceding steps before the RDS in pre-equilibrium or of the RDS, but not those of post-RDS according to the steady-state approximation [25,36]. Moreover, θ of the reaction intermediate for the RDS (*i.e.*, active species) increases with increasing OER overpotential and usually becomes dominant over those of preceding steps under OER operating potentials [37], enabling the selective observation of the active species during the OER using *in situ* spectroscopy analyses.

Nevertheless, there are also two limitations to observing active species by *in situ* spectroscopy. First, if the OER kinetics is too fast, relatively low-valence oxidized species are generated before the onset of the OER (outside the OER process) and can be detected instead of the active species [20]. Second, *in situ* oxidized but catalytically inactive species can be detected together with or instead of active species [32]. In this regard, it is necessary to confirm whether the observed oxidized species is an active species or not by checking the quantitative correlation between the amount of oxidized species and OER activity [3,12,33,38], or conducting control experiments to investigate the effects of experimental variables, such as electrolyte pH [11,19,29], isotope (*e.g.*, ^{18}O, ^{2}D)-labelling [4,11,14,32], and chemical probes [21], regarding the characteristics of the observed oxidized species as well as their correlation with the OER activity.

The amount of active species can be quantified based on the integrated area of their characteristic peaks from *in situ* spectroscopies. In addition, the amount of active species can be estimated from (1) pseudo-capacitive oxidative charge measured by pulse voltammetry [12], or (2) faradaic efficiency of the OER measured by a combination of differential electrochemical mass spectrometry (DEMS) and cyclic voltammetry [20,29].

Figure 1

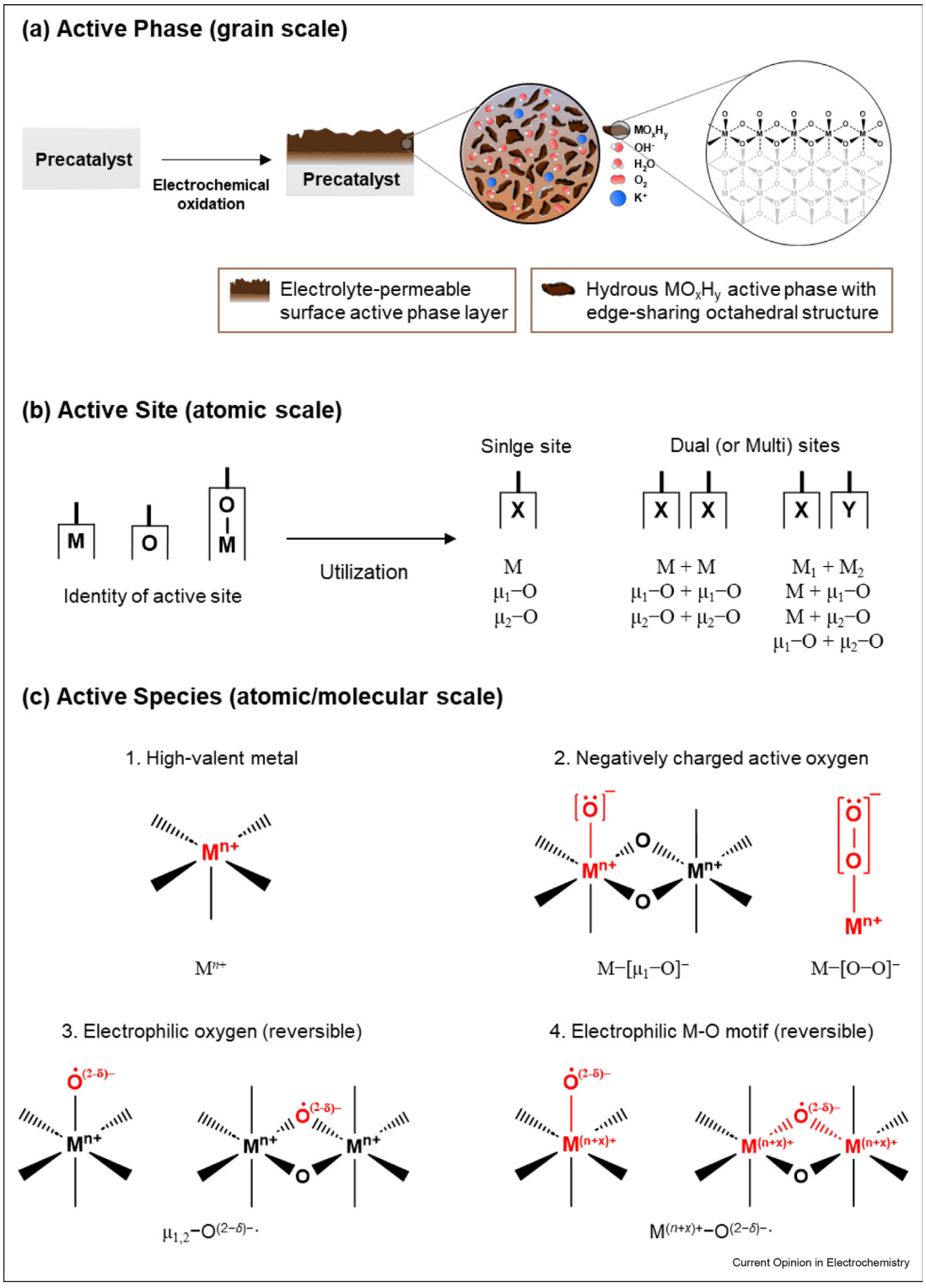

(a) Formation of the active phase on film/grain scale as a result of electrochemical oxidation and structure reconstruction of OER electrocatalysts. **(b)** Identity of three different types of OER active sites and utilization of active sites depending on the number and identity of active sites that participate in the OER. **(c)** Main types of active species for the OER.

However, caution should be taken in using these two methods as they can overestimate the amount of active species by measuring the low-valence oxidized species before the OER onset or the catalytically inactive oxidized species together with active species.

Main types of active species

The active species observed in MO_xH_y can be categorized into four different types according to their chemical structures and redox properties: (1) high-valence metal species (M^{n+}), (2) negatively charged active oxygen species (MOO^-), (3) electrophilic oxygen species or oxyl radical ($\mu_{1,2}-O^{(2-\delta)-}\cdot$), and (4) electrophilic M−O motif ($M^{(n+x)+}-O^{(2-\delta)-}\cdot$), where $0 < x$, $\delta \leq 1$, and μ_1−O and μ_2−O indicate terminal oxygen with one coordination and bridge oxygen with two coordination, respectively (Figure 1c).

First, the high-valence metal species are formed by oxidative deprotonation *via* proton-coupled electron transfer (PCET) with oxidation on the metal site. High-valence metal species have been detected by *in situ* X-ray absorption spectroscopy [14,24,27,39,40], *in situ* UV-Vis spectroscopy [41], and DEMS [20]. The RDS of the OER using high valence metal species is O−O bond formation.

Second, the negatively charged active oxygen species are further specified into two types: M−[μ_1−O]$^-$ and M−[O−O]$^-$. Note that the formal charge is used to assign the negative charge on the oxygen atom for negatively charged active oxygen species and both M−[μ_1−O]$^-$ and M−[O−O]$^-$ have eight electrons in total around each oxygen atom. M−[μ_1−O]$^-$ can be formed by (1) chemical deprotonation of MOOH to MOO^- (M−[μ_1−OH] + OH^- → M−[μ_1−O]$^-$ + H_2O) when the pH of the electrolyte is higher than the pK_a of MOOH [11,25,42], or (2) the super-Nernstian anodic redox reaction of $M(OH)_2$ (M^{2+}) to MOO^- ($M^{3+/4+}$) *via* decoupled proton/electron transfer (PT/ET) for Fe-doped MOOH (M = Ni and Co) [21,29], or hydrous MO_xH_y [43]. The presence of M−[μ_1−O]$^-$ as the active species has been confirmed by selectively blocking the negatively charged M−[μ_1−O]$^-$ with a positively charged polyatomic ion [21]. Its RDS during the OER is presumed to be the O−O bond formation step [11,21,29]. On the other hand, M−[O−O]$^-$ can be formed by PCET oxidation of M−[μ_1−O]$^-$ or deprotonation of M−[OOH] [11,19]. M−[O−O]$^-$ has been observed by *in situ* Raman spectroscopic analysis and the RDS of the OER using M−[O−O]$^-$ as the active species is expected to be the O_2 release step [4,11,19]. It is noted that M−[O−O]$^{n-}$−M (where $1 \leq n \leq 2$) can be formed by direct coupling of two μ_2−O species and be observed before the onset of the OER as a result of oxygen anion redox reaction or during the OER if RDS is an O_2 release step [4,10,44,45]. However, its negative charge is expressed based on the oxidation number instead of the formal charge as well as even its formal charge does not have a negative value. Hence, M−[O−O]$^{n-}$−M (where $1 \leq n \leq 2$) cannot be classified as a negatively charged active oxygen species.

Third, the electrophilic oxygen species is formed by oxidative deprotonation of the oxygen ligand of the MO_xH_y with no apparent oxidation of the metal site, and thus hole accumulation occurs on the oxygen ligand [13,26,38,46]. Fourth, the electrophilic M−O motif is formed by oxidative deprotonation with oxidation on both the metal and oxygen ligand [12,47]. Both electrophilic oxygen and M−O motif species have been identified by analyzing the oxidation state of the metal and oxygen employing *in situ* XANES (metal L-edge and oxygen K-edge) [12,47,48]. Also, their electrophilic character can improve the OER by facilitating the O−O bond formation step, which acts as the RDS [12,49]. It is noted that oxidation number is used to express the charge on oxygen for electrophilic oxygen and M−O motif species and the electrophilic oxygen species has less than eight electrons in total around the oxygen atom.

Electronic structure and redox center

Given that the identity of the active site and active species are closely related to the type of redox center (*e.g.*, metal, oxygen, and M−O motif), it is crucial to understand the origin of redox activity based on the electronic structure of the OER electrocatalyst. For the molecular orbital of edge-sharing octahedra of the MO_xH_y active phase, the (*M−O) anti-bonding orbital is filled with electrons from metal d orbitals and shows metallic character, while the (M−O) bonding orbital is filled with electrons from oxygen 2p orbitals and shows oxygen character [45,50]. When a conduction band made of (*M−O) anti-bonding orbital is partially filled with electrons, it splits into an empty upper Hubbard band (UHB) above the Fermi level (E_f) and a filled lower Hubbard band (LHB) below E_f according to Mott-Hubbard splitting [45,51].

Figure 2 shows three different types of electronic structures that determine the types of redox centers, which can potentially act as active sites. Figure 2a shows that when the LHB is located near E_f, the metal site can undergo an oxidative redox reaction from M^{n+} to $M^{(n+1)+}$ [45,52,53]. This is the case when only the metal acts as a redox center for the OER. However, excessive oxidation can make the LHB downshift and overlap with the band of the (M−O) bonding orbital, removing electrons from M−O bonding and destabilizing the MO_xH_y structure. Figure 2b shows that when the non-bonding oxygen band (O_{NB}) is formed and exists near the E_f alone, the oxygen ligand can show reversible redox behavior before the OER onset potential (E_{onset}), but irreversible oxidation

Figure 2

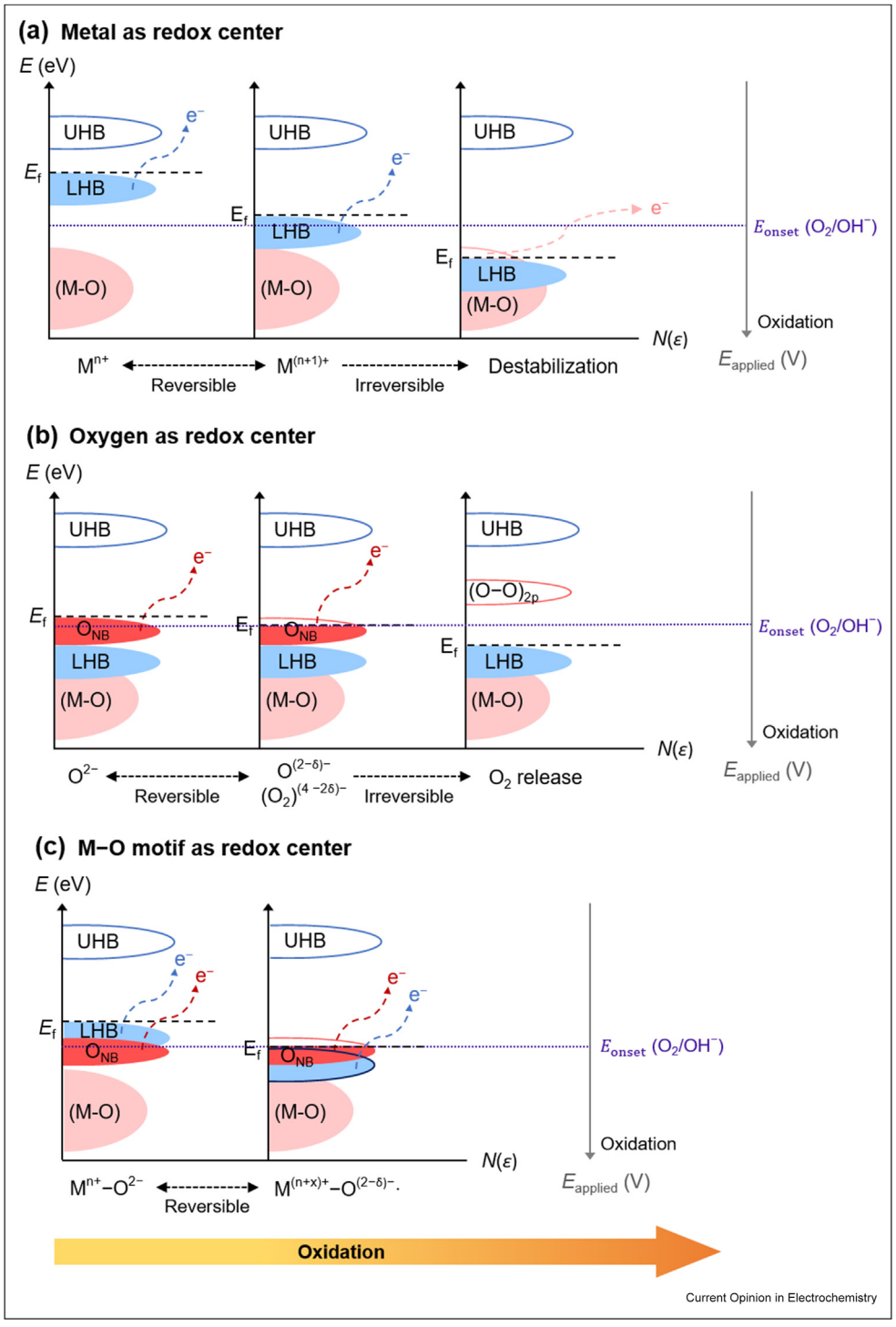

Schematic representation of the electronic band structure of 3d transition metal (oxy)hydroxides and its variation with oxidation for three different types of redox centers: **(a)** metal as redox center**, (b)** oxygen as redox center**,** and **(c)** M–O motif as redox center. The redox states of the redox centers and their redox reversibility are described below each electronic structure schematic. Here, E(eV) is the energy level, E_f is the Fermi level, $N(\varepsilon)$ is the density of states, $E_{applied}$(V) is the applied potential, E_{onset} (O_2/OH^-) is the OER onset potential, O_{NB} is the oxygen non-bonding states, (M–O) is the M–O bonding orbital band, $(O–O)_{2p}$ is the O–O hybridized band, and $0 \leq x, \delta \leq 1$.

(O_2 release) after E_{onset} [10,45]. Note, however, that the MO_xH_y structure can remain stable because the O 2p for M−O bonding does not participate in irreversible oxidation and O_2 release. Figure 2c shows that not only do LHB and O_{NB} overlap but also LHB exists (1) above the O_{NB} or (2) near the E_f even when the LHB is downshifted below O_{NB} after further oxidation [45,52,53]. In this case, both the metal and oxygen ligands can undergo reversible redox reactions sequentially *via* a reductive coupling mechanism or simultaneously [44,45], and the M−O motif as a whole is a redox center. Note that the M−O motif does not experience irreversible O_2 release even under OER potentials as opposed to the case in Figure 2b. This reversibility is due to the presence of the LHB near the E_f together with O_{NB}, which provides strong covalency between the metal and oxygen ligand so that the oxidized oxygen ligand can be maintained in the lattice even under OER potentials [44,45]. Moreover, for the same electronic structure of the M−O motif, only the reversible oxygen redox reaction without oxidation of the metal site can occur depending on the Fukui function [45,54]. Lastly, it is recommended to employ molecular orbital diagrams instead of atomic orbitals when studying the electronic structure of redox centers because molecular orbitals can exhibit Mott-Hubbard splitting and the presence of O_{NB}, which are critical factors determining the catalyst redox activity.

Driving force and reaction mechanism

Generally, an electrochemical reaction is accelerated by promoting the required electron transfer and the formation/breaking of chemical bonds. For a heterogeneous, inner-sphere electrochemical reaction, the applied potential can accelerate the rate of electrochemical reaction by (1) increasing θ of the active species on the catalyst or (2) changing the electrochemical potential of the catalyst or catalyst-reaction intermediates compared to that of products, thereby lowering the standard Gibbs free energy of activation ($\Delta G^{\ddagger}$) according to Eq. (1) [25,36,37]:

$$r = k^{\circ}\theta_a^m(a_{OH^-})\exp\left[\frac{-\Delta G^{\ddagger}}{RT}\right] \quad (1)$$

Here, r is the rate of electrochemical reaction, k^o is the standard rate constant, θ_a is the potential-dependent surface coverage of active species on the total number of active sites, m is the reaction order of the active species, a_{OH^-} is the activity of reactant OH^- and (a_{OH^-}) indicates that the a_{OH^-} term can be included or not depending on the presence of OH^- in the RDS, R is the ideal gas constant, and T is the temperature. The electrochemical potential of species j is defined as Eq. (2) [49]:

$$\overline{\mu}_j^{\alpha} = \mu_j^{\alpha} + z_j F\phi^{\alpha} \quad (2)$$

where $\overline{\mu}_j^{\alpha}$, μ_j^{α}, and ϕ^{α} are the electrochemical, chemical, and electrostatic potentials of species j in phase α, z_j is the charge number, and F is the Faraday constant. Equation (2) implies that not just electrostatic potential but also chemical potential can act as a driving force for the electrochemical reaction. Also, the driving force for multi-step (electro)chemical reactions like the OER is determined by the driving force for the RDS. When the RDS is an electrochemical reaction with charge transfer through an electrode or double layer *via* ion transfer (*e.g.*, proton), electrostatic potential is the main driving force, whereas the chemical potential is the driving force when the RDS is a chemical reaction [49].

Depending on the source of oxygen used for O−O bond formation, the OER mechanisms can be classified as either an adsorbate evolution mechanism (AEM) or lattice oxidation mechanism (LOM) [55−57]. For the AEM, the reactant from electrolyte (*e.g.*, OH^- or H_2O) is the only source of oxygen for O−O bond formation. On the other hand, for the LOM, one or two lattice oxygen atom(s) is the source of oxygen for O−O bond formation and released as O_2 gas. Therefore, according to the driving force and oxygen source for the OER, the reaction mechanism can be categorized into three different types: electrostatic potential-driven AEM (AEM-E), chemical potential-driven AEM (AEM-C), and LOM. Note that the LOM has electrostatic potential as the only driving force given its reported RDS (Table 1) [4,32,51,58−60]. Distinct characteristics of each mechanism will be addressed in terms of redox center, active site, active species, and RDS.

Conventionally, the OER has been believed to occur only *via* AEM-E [9]. In general, AEM-E occurs on a single active site and its RDS is an electrochemical O−O bond formation. AEM-E can have a redox center, such as metal or M−O motif, and active species, such as high-valence metal (M^{n+}) [24,27], negatively charged active oxygen species ($M-[\mu_1-O]^-$ or $M-[O-O]^-$) [11,19,21,29], and electrophilic M−O motif ($M^{(n+x)+}-O^{(2-\delta)-}\cdot$) [49], as summarized in Table 1.

The AEM-C has the following four key characteristics. First, the RDS is a chemical reaction. Given that O−O bond formation is the only reported RDS for AEM-C, AEM-C should have dual (or multiple) active sites for an O−O bond formation step to be a chemical reaction (Table 2) [12,14,26,47]. Second, O−O bond formation should occur on the μ_1−O site, not the μ_2−O site.

except for the triple active site case [12,14,26,38,46,47]. Third, the redox centers for AEM-C are identified as metal and M−O motif and possible active species are highly oxidized species including high-valence metal (M^{n+}) [14], electrophilic M−O motif ($M^{(n+x)+}-O^{(2-\delta)-}\cdot$) [12,47], or reversible electrophilic oxygen species ($\mu_{1,2}-O^{(2-\delta)-}\cdot$) [26,38,46]. Thus,

Table 1

Summary of the correlations between redox centers, active species, number of reaction sites, formation and consumption steps of active species, reaction mechanisms, and driving forces. Here, $0 \le x, \delta \le 1$. NA, DC, and OV denote nucleophilic attack, direct coupling, and oxygen vacancy, respectively. (M) implies that the metal site does not show redox activity during the OER and is not a component of active species.

Redox Center	Active Species	Preceding Step (Formation of Active Species)	Number of Reaction Sites	RDS (Consumption of Active Species)	Reaction Mechanism-Driving Force	Ref
M	M^{n+}	PCET oxidation	Single	O-O formation (NA)	AEM-E	[24,27]
			Dual (at RDS)	O-O formation (DC) : $\mu_1 = O + \mu_1 = O$	AEM-C	[14]
	$M–[\mu_1–O]^-$	PT/ET oxidation of $M(OH)_2$ to MOO^- Deprotonation of MOOH to MOO^-	Single	O-O formation (presumed)	AEM-E	[11,21,29]
	$M–[O–O]^-$	PCET oxidation of $M–[\mu_1–O]^-$ Deprotonation of M–[OOH]	Single	O_2 release	AEM-E	[11,19]
O	-	Regeneration of μ_2–OV	Single/Dual (after RDS)	Oxidative deprotonation of μ_2–OH to μ_2–O·	LOM-E	[58–60]
	μ_2–OOH (presumed)	O–O formation (NA) : μ_2–O· + OH^-	Single	Deprotonation of μ_2–OOH	LOM-E	[51]
	$\mu_2–[O–O]^-$ (presumed)	Deprotonation of μ_2–OOH	Single	O_2 release	LOM-E	[51]
	(M)–[O·–O]$^-$–(M)	O–O formation (DC) : μ_2–O· + μ_2–O	Dual (before RDS)	O_2 release	LOM-E	[4,32]
M–O	$M^{(n+x)+}–O^{(2-\delta)-}$·	Oxidative deprotonation of μ_1–OH with reversible oxidation on M and O	Single	O–O formation (NA)	AEM-E	[49]
			Dual (at RDS)	O–O formation (NA) :μ_1–O· +μ_2–O + reactant	AEM-C	[12,47]
	$(M^{n+})–\mu_2–O^{(2-\delta)-}$·	Oxidative deprotonation of $\mu_{1,2}$–OH with reversible oxidation on O	Triple (at RDS)	O–O formation (NA)	AEM-C	[38,46]
	$(M^{n+})–\mu_1–O^{(2-\delta)-}$·		Dual (at RDS)	O–O formation (DC) : μ_1–O· + μ_1–O·	AEM-C	[26]

Table 2

Classification of the O–O bond formation step depending on the reaction mechanism (AEM *vs.* LOM), the number of reaction sites (single site *vs.* dual sites), reaction pathways (nucleophilic attack *vs.* direct coupling), and the type of reaction for the O–O bond formation step (electrochemical *vs.* chemical). Here, μ_1-O and μ_2-O represent the reaction sites where the OER occurs, which can be different from the active site. Also, for simplicity, the notation of μ_1-O and μ_2-O do not contain information on the number of electrons (*e.g.*, formal charge or oxidation number), the (de)protonation, and the chemical bond property of the reaction site.

O–O bond formation step					
Reaction Mechanism	Reaction	Number of Reaction Sites	Pathway	Reaction Type	Ref
AEM	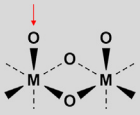 μ_1–O + Reactant	Single	Nucleophilic Attack	Electrochemical	[24,27]
	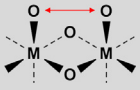 μ_1–O + μ_1–O	Dual	Direct Coupling	Chemical	[14,26]
	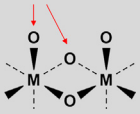 μ_1–O + μ_2–O + Reactant	Dual	Nucleophilic Attack	Chemical	[12,47]
LOM		Single	Nucleophilic Attack	Electrochemical	[42,51]
	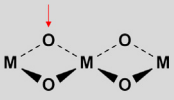 μ_2–O + Reactant	Dual	Direct Coupling	Chemical	[4,10,32]
	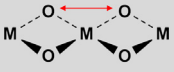 μ_2–O + μ_2–O	Dual	Direct Coupling	Chemical	[58,61]
	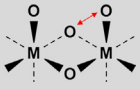 μ_2–O + μ_1–O				

electrocatalysts for AEM−C have the electronic structure of either Figure 2a or **c**. Table 1 summarizes various cases of AEM−C for different types of redox centers, active species, and pathways of formation and consumption of active species. Fourth, the θ_i should increase with increasing applied potential so that the activity of the OER with chemical RDS can be enhanced by increasing the applied potential.

AEM-C has two types depending on whether the θ_a affects $\Delta G^{\ddagger}$ for the RDS or not. For semiconducting OER (photo)electrocatalysts like Fe_2O_3, θ_a barely affects $\Delta G^{\ddagger}$ due to electronic localization [62,63]. Because each active species for inner-sphere, heterogeneous electrocatalysis is formed at different locations on the catalyst surface, these spatially separated active species have negligible interaction with each other (*i.e.*, no change of the enthalpy with θ_a). Therefore, the chemical potential of the active species (μ_{ads}) on the catalyst surface is independent of the θ_a. On the other hand, for conductive OER electrocatalysts like metallic IrO_x, spatially separated active species on the solvated catalyst surface can interact with each other due to Frumkin behavior and delocalize their redox states through the electrode. Therefore, the value of θ_a can change μ_{ads} as shown in Eq. (3) [12,63].

$$\mu_{ads} = \mu^{\circ}_{ads} + \gamma\theta_a \quad (3)$$

Here, μ^{o}_{ads} is the standard adsorption energy and γ is the Frumkin parameter. Note that μ_{ads} can be approximated as the enthalpy due to the negligible entropy term for heterogeneous, inner-sphere electrocatalysis [64], meaning that θ_a can change the enthalpy of reaction (ΔH_{rxn}) [12,63]. In addition, ΔH_{rxn} can modulate the Arrhenius activation energy (E_a) of the RDS according to the Brønsted–Evans–Polanyi (BEP) relation as shown in Eq. (4) [12,38]:

$$E_a = E_o + \alpha\Delta H_{rxn} \quad (4)$$

where E_o is the BEP intercept, and α is the BEP slope. Therefore, by combining Eqs. (3) and (4), the relationship between E_a and θ_a can be written as Eq. (5) [12]:

$$E_a = \zeta\theta_a + \kappa \quad (5)$$

where ζ and κ are constant coefficients. Note that E_a is approximately equal to the standard enthalpy of activation and the standard entropy of activation term often has a smaller magnitude compared to that of the standard enthalpy of activation [64,65]. This leads to the approximate relationship of $E_a \approx \Delta G^{\ddagger}$ for the RDS of heterogeneous, inner-sphere electrocatalysis.

The LOM is evidenced by the detection of lattice oxygen from released O_2 gas during the OER using isotope (^{18}O) labeling [10,66]. Compared to AEM, the LOM has the following distinct characteristics. First, at least one μ_2–O site should undergo irreversible oxidation and participate in O–O bond formation. For this process to occur, the oxygen redox center with the electronic structure shown in Figure 2b is involved in the LOM [10,45]. Note that electrophilic oxygen (or oxyl radical) that is formed and used for O–O bond formation during the LOM is different from the reversible electrophilic oxygen active species for the AEM-E/C in terms of its electronic structure and reversibility. Concerning the RDS and active species, the RDS of the LOM has been reported to be either the deprotonation of OH or OOH, or the O_2 release step, not the O–O bond formation step (Table 1). Thus, irreversible electrophilic oxygen that is used for O–O bond formation cannot be classified as an active species. Other catalyst–reaction intermediate surface complexes of the RDS, such as μ_2–[OOH], μ_2–$[OO]^-$, and (M)–$[O\cdot\text{–}O]^-$–(M) that do not belong to the main types of active species, can be classified as active species (Table 1). However, when the RDS is the deprotonation of lattice hydroxide (μ_2–OH), μ_2–OH is not termed an active species because μ_2–OH has not experienced any redox reaction or charge accumulation during the OER and θ for μ_2–OH does not have any impact on the resultant OER activity. The only driving force for the LOM is the electrostatic potential according to its RDS (Table 1) [4,32,51,58–60]. Also, though not an RDS for the LOM, O–O bond formation is still important because it determines the LOM pathways (Table 2) [4,10,32,42,51,58,61].

Role of applied potential and utilization of active species

Understanding the role of applied potential and utilization of active species in the OER process with reaction mechanisms involving different driving forces is critical in comprehending the origin of its kinetics. In this regard, how applied potential determines the rate of the OER is examined based on Eq. (1) consisting of the pre-exponential term including θ_a and the exponential term including $\Delta G^{\ddagger}$.

Regarding the pre-exponential term, θ_a is potential dependent regardless of the reaction mechanism and increases linearly or non-linearly with the applied potential depending on the density of states of the OER electrocatalyst [3,12,37]. This trend is observed because θ_a is determined by the formation and consumption of active species and the formation of active species is usually an electrochemical reaction regardless of the OER mechanism. For the exponential term, however, the role of applied potential changes with the driving force for the OER.

When the driving force for the OER is the electrostatic potential (*i.e.*, AEM-E and LOM), the applied potential can act on the reaction coordinate of the electrochemical RDS and change $\Delta G^{\ddagger}$ in the exponential term directly as shown in Eq. (6) [25,36,37].

$$i_{OER} = nFAk^{\circ}\theta_a^m(a_{OH^-})\exp\left[\frac{\beta F}{RT}\eta\right] \quad (6)$$

Here, i_{OER} is the steady-state OER current, n is the number of electrons transferred during the OER, which is four, A is the total number of active sites, β is the symmetry factor for the RDS, and η is the overpotential, which is the difference between applied and OER equilibrium potentials. Thus, the applied potential can enhance the OER by affecting both pre-exponential and exponential terms directly.

For the AEM-C, the applied potential cannot directly act on the reaction coordinate of the RDS and thus has no direct effect on $\Delta G^{\ddagger}$. However, depending on the type of AEM-C, $\Delta G^{\ddagger}$ (or E_a) can have a potential dependence. For AEM-C without Frumkin behavior, the chemical potential driving force and $\Delta G^{\ddagger}$ for AEM-C have fixed values, which are determined by characteristics of a given chemical reaction, electrocatalyst, and

electrolyte. Hence, the applied potential enhances the OER by affecting θ_a in the pre-exponential term according to Eq. (7) [25,36,37].

$$i_{\mathrm{OER}} = nFAk^{\circ}\theta_a^m(a_{OH^-})\exp\left[\frac{-\Delta G^{\ddagger}}{RT}\right] \quad (7)$$

In contrast, θ_a can affect E_a in AEM-C *via* Frumkin behavior, according to Eq. (5). Thus, the applied potential can enhance the OER by affecting not just the pre-exponential term but also the exponential term indirectly *via* the effect of θ_a on E_a as shown in Eq. (8) [12,25,36,37].

$$i_{\mathrm{OER}} = nFAk^{\circ}\theta_a^m(a_{OH^-})\exp\left[\frac{\zeta\theta_a + \kappa}{RT}\right] \quad (8)$$

According to Eq. (6)−(8), the relationship between i_{OER} and η, or between i_{OER} and θ_a can be used to discern the OER mechanisms with different driving forces. For example, when i_{OER} has an exponential dependence on η (*i.e.*, a linear Tafel slope of η against $\log[i_{\mathrm{OER}}]$), it is presumed that OER occurs *via* electrostatic potential-driven mechanisms like the AEM-E and the LOM [49]. For the AEM-C, the relationship between i_{OER} and θ_a is used instead of that between i_{OER} and η. If i_{OER} has a power-law relationship with θ_a (*i.e.*, a linear relationship between $\log[i_{\mathrm{OER}}]$ and $\log[\theta_a]$), the OER occurs *via* the AEM-C without Frumkin behavior [3,38,46]. On the other hand, if i_{OER} has an exponential dependence on θ_a, it is suggested that the OER occurs *via* AEM-C with Frumkin behavior [12,14]. Note, however, that the interpretation of this relationship has limitations; if θ_a in the pre-exponential term has a significant value compared to the exponential term, the relationship of i_{OER} and η for AEM-E and LOM, and that of i_{OER} and θ_a for AEM-C with the Frumkin behavior can deviate from exponential dependence. Also, if θ_a increases linearly with the applied potential as in the case for IrO_x, and if it has only one type of active species, the AEM-C with Frumkin behavior can also show exponential dependence for i_{OER} on η (*i.e.*, linear Tafel slope) even though the driving force is not the electrostatic potential.

Conclusion and outlook

In this review, the key concepts for understanding the OER at the atomic/molecular scale are reviewed, including the active phase, active site, active species, redox center, electronic structure, reaction mechanism and pathway, driving force, and RDS. These concepts were categorized according to their unique characteristics and the correlation between each concept was systematically discussed. This review aims to provide an overall picture of the OER at the atomic/molecular scale that will help understand the complexity of the OER.

To address the remaining ambiguities and improve the understanding of these concepts, some critical research questions are raised below. First, it is necessary to develop a better understanding of the different types of active oxygen species in terms of their identity, formation, and consumption. In terms of identity, for example, three different types of active oxygen species (*i.e.*, M−$[\mu_1{-}O]^-$, M−$[O{-}O]^-$, $\mu_{1,2}{-}O^-\cdot$) were reported for NiFe-based (oxy)hydroxide electrocatalysts depending on the experimental methods, such as *in situ* XAFS, *in situ* Raman spectroscopy, *in situ* UV-Vis, pH effect, and chemical probe [13,19,21,29,32,33]. The reason for the observation of different active species should be clarified whether it is due to different material properties with different reaction mechanisms and RDS, or the limitation of each experimental method. In terms of the formation of active species, three different types of active species have common characteristics in that they all appear at pre-catalytic potential, especially near the anodic redox potential for M^{2+} in MO_xH_y, implying the possibility that they have similar formation principles or are related to each other. In terms of consumption of active species, given that the electrophilic oxygen species is favorable for O−O bond formation, it is unclear how M−$[\mu_1{-}O]^-$ with an eight electron configuration and nucleophilic character can act as the active species for the same RDS (*i.e.*, O−O bond formation).

Second, given that there are few reports on AEM-C for alkaline OER electrocatalysts, further investigation is needed to determine which electrocatalysts promote the OER *via* AEM-C and to understand whether they show Frumkin behavior or not in terms of their material properties, such as electrical conductivity and the resulting degree of (de)localization of redox states of active species. For example, NiFeOOH and $\alpha{-}Fe_2O_3$ OER (photo) electrocatalysts have shown AEM-C without significant change in the value of E_a [3,38,46], whereas NiFe layered double hydroxide from another study, whose active phase is the same as NiFeOOH, has shown AEM-C with a notable change in the value of E_a [12].

Third, different reaction mechanisms can be observed for one electrocatalyst at the same time. This phenomenon needs to be clarified by investigating (1) if complicated electronic structures can induce two reaction mechanisms at the same time (which is presumably related to the defects formed during the synthesis of the electrocatalyst or the OER), or (2) if the potential-dependent modulation of the chemical and electronic structure through the oxidation or the ion exchange with the electrolyte results in the reaction mechanism change [36,47].

Declaration of competing interest

The authors declare the following financial interests/personal relationships which may be considered as

potential competing interests: Charles Buddie Mullins reports financial support was provided by National Science Foundation. Charles Buddie Mullins reports financial support was provided by Welch Foundation.

Data availability

Data used for writing this review is from published journal articles.

Acknowledgments

This work was supported by the National Science Foundation [grant number CHE-2102307]; and the Welch Foundation, Houston, TX [grant number F-1436].

References

Papers of particular interest, published within the period of review, have been highlighted as:

* of special interest
** of outstanding interest

1. Seitz LC, Dickens CF, Nishio K, Hikita Y, Montoya J, Doyle A, Kirk C, Vojvodic A, Hwang HY, Norskov JK, Jaramillo TF: **A highly active and stable IrO_x/$SrIrO_3$ catalyst for the oxygen evolution reaction**. *Science* 2016, **353**:1011–1014, https://doi.org/10.1126/science.aaf5050.

2. Laha S, Lee Y, Podjaski F, Weber D, Duppel V, Schoop LM, Pielnhofer F, Scheurer C, Müller K, Starke U, Reuter K, Lotsch BV: **Ruthenium oxide nanosheets for enhanced oxygen evolution catalysis in acidic medium**. *Adv Energy Mater* 2019, **9**, 1803795, https://doi.org/10.1002/aenm.201803795.

3. * Francàs L, Corby S, Selim S, Lee D, Mesa CA, Godin R, Pastor E, Stephens IEL, Choi K-S, Durrant JR: **Spectroelectrochemical study of water oxidation on nickel and iron oxyhydroxide electrocatalysts**. *Nat Commun* 2019, **10**:5208, https://doi.org/10.1038/s41467-019-13061-0.
in situ UV-Vis spectroscopy is used to quantify the potential-dependent generation of the oxidized active species during the OER. A quantitative correlation between the surface density of oxidized active species, applied bias, and the OER activity was studied, proving that applied bias is mainly used to generate the oxidized active species, and active species is chemically consumed at the RDS of the OER.

4. * Moysiadou A, Lee S, Hsu C-S, Chen HM, Hu X: **Mechanism of oxygen evolution catalyzed by cobalt oxyhydroxide: cobalt superoxide species as a key intermediate and dioxygen release as a rate-determining step**. *J Am Chem Soc* 2020, **142**:11901–11914, https://doi.org/10.1021/jacs.0c04867.
Operando XAS and Raman spectroscopy analyses show the resting state of CoO_2 with Co^{4+} oxidation state before the OER and the presence of superoxidic oxygen species as active species. As opposed to previously reported negatively charged oxygen species for AEM, electrophilic oxygen redox center is used to create the superoxidic oxygen active species *via* LOM and O_2 release was revealed as the RDS of the OER for superoxidic active oxygen species.

5. Son YJ, Kawashima K, Wygant BR, Lam CH, Burrow JN, Celio H, Dolocan A, Ekerdt JG, Mullins CB: **Anodized nickel foam for oxygen evolution reaction in fe-free and unpurified alkaline electrolytes at high current densities**. *ACS Nano* 2021, **15**:3468–3480, https://doi.org/10.1021/acsnano.0c10788.

6. Peugeot A, Creissen CE, Karapinar D, Tran HN, Schreiber M, Fontecave M: **Benchmarking of oxygen evolution catalysts on porous nickel supports**. *Joule* 2021, **5**:1281–1300, https://doi.org/10.1016/j.joule.2021.03.022.

7. Liang C, Zou P, Nairan A, Zhang Y, Liu J, Liu K, Hu S, Kang F, Fan HJ, Yang C: **Exceptional performance of hierarchical Ni–Fe oxyhydroxide@NiFe alloy nanowire array electrocatalysts for large current density water splitting**. *Energy Environ Sci* 2020, **13**:86–95, https://doi.org/10.1039/C9EE02388G.

8. Shang H, Liu D: **Atomic design of carbon-based dual-metal site catalysts for energy applications**. *Nano Res* 2023, **16**:1913–1966, https://doi.org/10.1007/s12274-023-5449-9.

9. Rossmeisl J, Qu Z-W, Zhu H, Kroes G-J, Nørskov JK: **Electrolysis of water on oxide surfaces**. *J Electroanal Chem* 2007, **607**:83–89, https://doi.org/10.1016/j.jelechem.2006.11.008.

10. Grimaud A, Hong WT, Shao-Horn Y, Tarascon J-M: **Anionic redox processes for electrochemical devices**. *Nat Mater* 2016, **15**:121–126, https://doi.org/10.1038/nmat4551.

11. Diaz-Morales O, Ferrus-Suspedra D, Koper MTM: **The importance of nickel oxyhydroxide deprotonation on its activity towards electrochemical water oxidation**. *Chem Sci* 2016, **7**:2639–2645, https://doi.org/10.1039/C5SC04486C.

12. ** Nong HN, Falling LJ, Bergmann A, Klingenhof M, Tran HP, Spöri C, Mom R, Timoshenko J, Zichittella G, Knop-Gericke A, Piccinin S, Pérez-Ramírez J, Cuenya BR, Schlögl R, Strasser P, Teschner D, Jones TE: **Key role of chemistry versus bias in electrocatalytic oxygen evolution**. *Nature* 2020, **587**:408–413, https://doi.org/10.1038/s41586-020-2908-2.
By integrating electrochemical analysis and *operando* XAS, this work revealed that oxidative deprotonation of IrO_x during the OER accumulates holes on the M–O motif. Also, exponential dependence of the OER activity of metallic IrO_x on hole accumulation was observed. DFT calculations explain that OER is driven by the chemical potential instead of electrostatic potential and the activation energy of the OER can also be modulated by potential-dependent hole accumulation.

13. * Drevon D, Görlin M, Chernev P, Xi L, Dau H, Lange KM: **Uncovering the role of oxygen in Ni-Fe(oxhy) electrocatalysts using in situ soft X-ray absorption spectroscopy during the oxygen evolution reaction**. *Sci Rep* 2019, **9**:1532, https://doi.org/10.1038/s41598-018-37307-x.
In situ XAS at oxygen K-edge together with electrochemical analysis revealed that hole accumulation occurs for Ni-FeO_xH_y electrocatalyst during the OER by oxidation of not just metal sites but also oxygen sites, forming partially oxidized oxygen sites.

14. Pasquini C, Zaharieva I, González-Flores D, Chernev P, Mohammadi MR, Guidoni L, Smith RDL, Dau H: **H/D isotope effects reveal factors controlling catalytic activity in Co-based oxides for water oxidation**. *J Am Chem Soc* 2019, **141**:2938–2948, https://doi.org/10.1021/jacs.8b10002.

15. Wygant BR, Kawashima K, Mullins CB: **Catalyst or precatalyst? The effect of oxidation on transition metal carbide, pnictide, and chalcogenide oxygen evolution catalysts**. *ACS Energy Lett* 2018, **3**:2956–2966, https://doi.org/10.1021/acsenergylett.8b01774.

16. Son YJ, Kim S, Leung V, Kawashima K, Noh J, Kim K, Marquez RA, Carrasco-Jaim OA, Smith LA, Celio H, Milliron DJ, Korgel BA, Mullins CB: **Effects of electrochemical conditioning on nickel-based oxygen evolution electrocatalysts**. *ACS Catal* 2022, **12**:10384–10399, https://doi.org/10.1021/acscatal.2c01001.

17. Lopes PP, Chung DY, Rui X, Zheng H, He H, Farinazzo Bergamo Dias Martins P, Strmcnik D, Stamenkovic VR, Zapol P, Mitchell JF, Klie RF, Markovic NM: **Dynamically stable active sites from surface evolution of perovskite materials during the oxygen evolution reaction**. *J Am Chem Soc* 2021, **143**:2741–2750, https://doi.org/10.1021/jacs.0c08959.

18. May KJ, Carlton CE, Stoerzinger KA, Risch M, Suntivich J, Lee Y-L, Grimaud A, Shao-Horn Y: **Influence of oxygen evolution during water oxidation on the surface of perovskite oxide catalysts**. *J Phys Chem Lett* 2012, **3**:3264–3270, https://doi.org/10.1021/jz301414z.

19. Trześniewski BJ, Diaz-Morales O, Vermaas DA, Longo A, Bras W, Koper MTM, Smith WA: **In situ observation of active oxygen species in Fe-containing Ni-based oxygen evolution catalysts: the effect of pH on electrochemical activity**. *J Am Chem Soc* 2015, **137**:15112–15121, https://doi.org/10.1021/jacs.5b06814.

20. Görlin M, Chernev P, Ferreira de Araújo J, Reier T, Dresp S, Paul B, Krähnert R, Dau H, Strasser P: **Oxygen evolution reaction dynamics, faradaic charge efficiency, and the active metal redox states of Ni–Fe oxide water splitting electrocatalysts**. *J Am Chem Soc* 2015, **138**:5603–5614, https://doi.org/10.1021/jacs.6b00332.

21. Yang C, Fontaine O, Tarascon J-M, Grimaud A: **Chemical recognition of active oxygen species on the surface of oxygen evolution reaction electrocatalysts**. *Angew Chem Int Ed* 2017, **56**:8652–8656, https://doi.org/10.1002/anie.201701984.

22. Bai X, Duan Z, Nan B, Wang L, Tang T, Guan J: **Unveiling the active sites of ultrathin Co-Fe layered double hydroxides for the oxygen evolution reaction**. *Chin J Catal* 2022, **43**:2240–2248, https://doi.org/10.1016/S1872-2067(21)64033-0.

23. Smith RDL, Pasquini C, Loos S, Chernev P, Klingan K, Kubella P, Mohammadi MR, Gonzalez-Flores D, Dau H: **Spectroscopic identification of active sites for the oxygen evolution reaction on iron-cobalt oxides**. *Nat Commun* 2017, **8**:2022, https://doi.org/10.1038/s41467-017-01949-8.

24. Enman LJ, Stevens MB, Dahan MH, Nellist MR, Toroker MC, Boettcher SW: **Operando X-ray absorption spectroscopy shows iron oxidation is concurrent with oxygen evolution in cobalt–iron (oxy)hydroxide electrocatalysts**. *Angew Chem* 2018, **130**:13022–13026, https://doi.org/10.1002/ange.201808818.

25. Bediako DK, Surendranath Y, Nocera DG: **Mechanistic studies of the oxygen evolution reaction mediated by a nickel–borate thin film electrocatalyst**. *J Am Chem Soc* 2013, **135**:3662–3674, https://doi.org/10.1021/ja3126432.

26. Ullman AM, Brodsky CN, Li N, Zheng S-L, Nocera DG: **Probing edge site reactivity of oxidic cobalt water oxidation catalysts**. *J Am Chem Soc* 2016, **138**:4229–4236, https://doi.org/10.1021/jacs.6b00762.

27. Friebel D, Louie MW, Bajdich M, Sanwald KE, Cai Y, Wise AM, Cheng M-J, Sokaras D, Weng T-C, Alonso-Mori R, Davis RC, Bargar JR, Nørskov JK, Nilsson A, Bell AT: **Identification of highly active Fe sites in (Ni,Fe)OOH for electrocatalytic water splitting**. *J Am Chem Soc* 2015, **137**:1305–1313, https://doi.org/10.1021/ja511559d.

28. Ahn HS, Bard AJ: **Surface interrogation scanning electrochemical microscopy of $Ni_{1-x}Fe_xOOH$ ($0 < x < 0.27$) oxygen evolving catalyst: kinetics of the "fast" iron sites**. *J Am Chem Soc* 2016, **138**:313–318, https://doi.org/10.1021/jacs.5b10977.

29. Görlin M, Ferreira de Araújo J, Schmies H, Bernsmeier D, Dresp S, Gliech M, Jusys Z, Chernev P, Kraehnert R, Dau H, Strasser P: **Tracking catalyst redox states and reaction dynamics in Ni–Fe oxyhydroxide oxygen evolution reaction electrocatalysts: the role of catalyst support and electrolyte pH**. *J Am Chem Soc* 2017, **139**:2070–2082, https://doi.org/10.1021/jacs.6b12250.

30. Rao RR, Corby S, Bucci A, García-Tecedor M, Mesa CA, Rossmeisl J, Giménez S, Lloret-Fillol J, Stephens IEL, Durrant JR: **Spectroelectrochemical analysis of the water oxidation mechanism on doped nickel oxides**. *J Am Chem Soc* 2022, **144**:7622–7633, https://doi.org/10.1021/jacs.1c08152.

31. Lee S, Chu Y-C, Bai L, Chen HM, Hu X: **Operando identification of a side-on nickel superoxide intermediate and the mechanism of oxygen evolution on nickel oxyhydroxide**. *Chem Catal* 2023, **3**, 100475, https://doi.org/10.1016/j.checat.2022.11.014.

32. Lee S, Banjac K, Lingenfelder M, Hu X: **Oxygen isotope labeling experiments reveal different reaction sites for the oxygen evolution reaction on nickel and nickel iron oxides**. *Angew Chem Int Ed* 2019, **58**:10295–10299, https://doi.org/10.1002/anie.201903200.

33. Hu C, Hu Y, Fan C, Yang L, Zhang Y, Li H, Xie W: **Surface-enhanced Raman spectroscopic evidence of key intermediate species and role of NiFe dual-catalytic center in water oxidation**. *Angew Chem Int Ed* 2021, **60**:19774–19778, https://doi.org/10.1002/anie.202103888.

34. Ali-Löytty H, Louie MW, Singh MR, Li L, Sanchez Casalongue HG, Ogasawara H, Crumlin EJ, Liu Z, Bell AT, Nilsson A, Friebel D: **Ambient-pressure XPS study of a Ni–Fe electrocatalyst for the oxygen evolution reaction**. *J Phys Chem C* 2016, **120**:2247–2253, https://doi.org/10.1021/acs.jpcc.5b10931.

35. Mom RV, Falling LJ, Kasian O, Algara-Siller G, Teschner D, Crabtree RH, Knop-Gericke A, Mayrhofer KJJ, Velasco-Vélez J-J, Jones TE: **Operando structure–activity–stability relationship of iridium oxides during the oxygen evolution reaction**. *ACS Catal* 2022, **12**:5174–5184, https://doi.org/10.1021/acscatal.1c05951.

36. Mefford JT, Zhao Z, Bajdich M, Chueh WC: **Interpreting Tafel behavior of consecutive electrochemical reactions through combined thermodynamic and steady state microkinetic approaches**. *Energy Environ Sci* 2020, **13**:622–634, https://doi.org/10.1039/C9EE02697E.

37. Shinagawa T, Garcia-Esparza AT, Takanabe K: **Insight on Tafel slopes from a microkinetic analysis of aqueous electrocatalysis for energy conversion**. *Sci Rep* 2015, **5**, 13801, https://doi.org/10.1038/srep13801.

38. ** Righi G, Plescher J, Schmidt F-P, Campen RK, Fabris S, Knop-Gericke A, Schlögl R, Jones TE, Teschner D, Piccinin S: **On the origin of multihole oxygen evolution in haematite photoanodes**. *Nat Catal* 2022, **5**:888–899, https://doi.org/10.1038/s41929-022-00845-9.
By integrating electrochemical analysis, DFT calculations, and microkinetic modeling, this work shows the power law dependence of the OER activity of semiconducting α–Fe_2O_3 on the surface hole density. This result indicates that applied potential determines the OER activity mainly by controlling the surface density of the oxyl radical active species, not changing its activation energy.

39. Risch M, Ringleb F, Kohlhoff M, Bogdanoff P, Chernev P, Zaharieva I, Dau H: **Water oxidation by amorphous cobalt-based oxides: in situ tracking of redox transitions and mode of catalysis**. *Energy Environ Sci* 2015, **8**:661–674, https://doi.org/10.1039/C4EE03004D.

40. Bediako DK, Lassalle-Kaiser B, Surendranath Y, Yano J, Yachandra VK, Nocera DG: **Structure–activity correlations in a nickel–borate oxygen evolution catalyst**. *J Am Chem Soc* 2012, **134**:6801–6809, https://doi.org/10.1021/ja301018q.

41. Goldsmith ZK, Harshan AK, Gerken JB, Vörös M, Galli G, Stahl SS, Hammes-Schiffer S: **Characterization of NiFe oxyhydroxide electrocatalysts by integrated electronic structure calculations and spectroelectrochemistry**. *Proc Natl Acad Sci USA* 2017, **114**:3050–3055, https://doi.org/10.1073/pnas.1702081114.

42. Huang Z-F, Xi S, Song J, Dou S, Li X, Du Y, Diao C, Xu ZJ, Wang X: **Tuning of lattice oxygen reactivity and scaling relation to construct better oxygen evolution electrocatalyst**. *Nat Commun* 2021, **12**:3992, https://doi.org/10.1038/s41467-021-24182-w.

43. Doyle RL, Godwin IJ, Brandon MP, Lyons MEG: **Redox and electrochemical water splitting catalytic properties of hydrated metal oxide modified electrodes**. *Phys Chem Chem Phys* 2013, **15**:13737–13783, https://doi.org/10.1039/C3CP51213D.

44. Saubanère M, McCalla E, Tarascon J-M, Doublet M-L: **The intriguing question of anionic redox in high-energy density cathodes for Li-ion batteries**. *Energy Environ Sci* 2016, **9**:984–991, https://doi.org/10.1039/C5EE03048J.

45. Assat G, Tarascon J-M: **Fundamental understanding and practical challenges of anionic redox activity in Li-ion batteries**. *Nat Energy* 2018, **3**:373–386, https://doi.org/10.1038/s41560-018-0097-0.

46. Mesa CA, Francàs L, Yang KR, Garrido-Barros P, Pastor E, Ma Y, Kafizas A, Rosser TE, Mayer MT, Reisner E, Grätzel M, Batista VS, Durrant JR: **Multihole water oxidation catalysis on haematite photoanodes revealed by operando spectroelectrochemistry and DFT**. *Nat Chem* 2020, **12**:82–89, https://doi.org/10.1038/s41557-019-0347-1.

47. Bergmann A, Jones TE, Martinez Moreno E, Teschner D, Chernev P, Gliech M, Reier T, Dau H, Strasser P: **Unified structural motifs of the catalytically active state of Co(oxyhydr)oxides during the electrochemical oxygen evolution reaction**. *Nat Catal* 2018, **1**:711–719, https://doi.org/10.1038/s41929-018-0141-2.

48. Grimaud A, Demortière A, Saubanère M, Dachraoui W, Duchamp M, Doublet M-L, Tarascon J-M: **Activation of surface**

oxygen sites on an iridium-based model catalyst for the oxygen evolution reaction. *Nat Energy* 2016, **2**:1–10, https://doi.org/10.1038/nenergy.2016.189.

49. Boettcher SW, Surendranath Y: **Heterogeneous electrocatalysis goes chemical**. *Nat Catal* 2021, **4**:4–5, https://doi.org/10.1038/s41929-020-00570-1.

50. Li N, Bediako DK, Hadt RG, Hayes D, Kempa TJ, von Cube F, Bell DC, Chen LX, Nocera DG: **Influence of iron doping on tetravalent nickel content in catalytic oxygen evolving films**. *Proc Natl Acad Sci USA* 2017, **114**:1486–1491, https://doi.org/10.1073/pnas.1620787114.

51. He Z, Zhang J, Gong Z, Lei H, Zhou D, Zhang N, Mai W, Zhao S, Chen Y: **Activating lattice oxygen in NiFe-based (oxy)hydroxide for water electrolysis**. *Nat Commun* 2022, **13**:2191, https://doi.org/10.1038/s41467-022-29875-4.

52. Huang Z-F, Song J, Du Y, Xi S, Dou S, Nsanzimana JMV, Wang C, Xu ZJ, Wang X: **Chemical and structural origin of lattice oxygen oxidation in Co–Zn oxyhydroxide oxygen evolution electrocatalysts**. *Nat Energy* 2019, **4**:329–338, https://doi.org/10.1038/s41560-019-0355-9.

53. Wang X, Xi S, Huang P, Du Y, Zhong H, Wang Q, Borgna A, Zhang Y-W, Wang Z, Wang H, Yu ZG, Lee WSV, Xue J: **Pivotal role of reversible NiO6 geometric conversion in oxygen evolution**. *Nature* 2022, **611**:702–708, https://doi.org/10.1038/s41586-022-05296-7.

54. McCalla E, Abakumov AM, Saubanère M, Foix D, Berg EJ, Rousse G, Doublet M-L, Gonbeau D, Novák P, Van Tendeloo G, Dominko R, Tarascon J-M: **Visualization of O-O peroxo-like dimers in high-capacity layered oxides for Li-ion batteries**. *Science* 2015, **350**:1516–1521, https://doi.org/10.1126/science.aac8260.

55. Liang Q, Brocks G, Bieberle-Hütter A: **Oxygen evolution reaction (OER) mechanism under alkaline and acidic conditions**. *J Phys Energy* 2021, **3**, 026001, https://doi.org/10.1088/2515-7655/abdc85.

56. Tang M, Ge Q: **Mechanistic understanding on oxygen evolution reaction on γ-FeOOH (010) under alkaline condition based on DFT computational study**. *Chin J Catal* 2017, **38**:1621–1628, https://doi.org/10.1016/S1872-2067(17)62760-8.

57. Wang X, Zhong H, Xi S, Lee WSV, Xue J: **Understanding of oxygen redox in the oxygen evolution reaction**. *Adv Mater* 2022, **34**, 2107956, https://doi.org/10.1002/adma.202107956.

58. Mefford JT, Rong X, Abakumov AM, Hardin WG, Dai S, Kolpak AM, Johnston KP, Stevenson KJ: **Water electrolysis on La1−xSrxCoO3−δ perovskite electrocatalysts**. *Nat Commun* 2016, **7**, 11053, https://doi.org/10.1038/ncomms11053.

59. Grimaud A, Diaz-Morales O, Han B, Hong WT, Lee Y-L, Giordano L, Stoerzinger KA, Koper MTM, Shao-Horn Y: **Activating lattice oxygen redox reactions in metal oxides to catalyse oxygen evolution**. *Nat Chem* 2017, **9**:457–465, https://doi.org/10.1038/nchem.2695.

60. Sun Y, Liao H, Wang J, Chen B, Sun S, Ong SJH, Xi S, Diao C, Du Y, Wang J-O, Breese MBH, Li S, Zhang H, Xu ZJ: **Covalency competition dominates the water oxidation structure–activity relationship on spinel oxides**. *Nat Catal* 2020, **3**:554–563, https://doi.org/10.1038/s41929-020-0465-6.

61. Yoo JS, Rong X, Liu Y, Kolpak AM: **Role of lattice oxygen participation in understanding trends in the oxygen evolution reaction on perovskites**. *ACS Catal* 2018, **8**:4628–4636, https://doi.org/10.1021/acscatal.8b00612.

62. Rao RR, Stephens IEL, Durrant JR: **Understanding what controls the rate of electrochemical oxygen evolution**. *Joule* 2021, **5**:16–18, https://doi.org/10.1016/j.joule.2020.12.017.

63. Schmickler W, Santos E: *Interfacial electrochemistry*. Berlin, Heidelberg: Springer; 2010, https://doi.org/10.1007/978-3-642-04937-8.

64. Resasco J, Abild-Pedersen F, Hahn C, Bao Z, Koper MTM, Jaramillo TF: **Enhancing the connection between computation and experiments in electrocatalysis**. *Nat Catal* 2022, **5**:374–381, https://doi.org/10.1038/s41929-022-00789-0.

65. Bard AJ, Faulkner LR, White HS: *Electrochemical methods: fundamentals and applications*. 3rd ed. New York: Wiley; 2022.

66. Ferreira de Araújo J, Dionigi F, Merzdorf T, Oh H-S, Strasser P: **Evidence of Mars-Van-Krevelen mechanism in the electrochemical oxygen evolution on Ni-based catalysts**. *Angew Chem Int Ed* 2021, **60**:14981–14988, https://doi.org/10.1002/anie.202101698.